Polarization-Multiplexed Metasurface Integrating Transmissive Vortex Beam Generation and Monostatic RCS Reduction

(Article begins on next page)

This article has been accepted for publication in IEEE Open Journal of Antennas and Propagation. This is the author's version which has not been fully edited and content may change prior to final publication. Citation information: DOI 10.1109/OJAP.2026.3729779

Received XX Month XXXX; revised X Month XXXX; accepted XX Month XXXX. Date of publication XX Month XXXX; date of current version XX Month XXXX.

Digital Object Identifier

Polarization-Multiplexed Metasurface Integrating Transmissive Vortex Beam Generation and Monostatic RCS Reduction

Zhaohua Li,[1] Yu Zhang,[2,*] Yuxin Ren,[2] and Junhong Wang[1]

[1] The Key Laboratory of All Optical Network and Advanced Telecommunication Network, Ministry of Education, Institute of Lightwave Technology, Beijing Jiaotong University, Beijing 100044, China

[2] The China Academy of Information and Communications Technology, Beijing 100191, China

CORRESPONDING AUTHOR: Yu Zhang (e-mail: zhangyu5@caict.ac.cn).

This work was supported by the National Natural Science Foundation of China under Grant U2241204.

ABSTRACT Integrating transmissive orbital angular momentum (OAM) beam generation and reflective monostatic radar cross section (RCS) reduction within a single aperture remains challenging because the two functions require distinct transmission and reflection phase responses. This paper proposes a polarization-multiplexed metasurface based on a multilayer anisotropic unit cell and a unified phase-superposition strategy. In the transmission channel, the vortex phase is combined with a beam-steering phase to generate OAM beams propagating along the normal or a prescribed deflected direction. In the reflection channel, the diffusion phase is superimposed with the vortex phase to redistribute the reflected energy and suppress the broadside backscattering. Depending on the polarization and propagation direction of the incident wave, the same aperture generates transmissive OAM beams with topological charges of +3 and −3 or performs monostatic RCS reduction. Full-wave modal analyses verify the designed OAM states, while measurements confirm the corresponding beam and scattering characteristics. Under normally incident y-polarized waves, the measured RCS reduction exceeds 10 dB from 12.4 GHz to 15.6 GHz, corresponding to a relative bandwidth of 22.8%, with a peak reduction of 30.15 dB at 13.3 GHz. Under normally incident x-polarized waves, the measured RCS reduction is approximately 15–24 dB from 11 GHz to 16 GHz. These results demonstrate the feasibility of integrating direction-dependent OAM transmission and polarization-dependent RCS reduction within a single metasurface aperture.

INDEX TERMS metasurface, multifunction, orbital angular momentum, phase superposition, RCS reduction

I. INTRODUCTION

With rapid advancement of radar and communication technologies, airborne platforms are required to have both high-channel-capacity communication between inside and outside and strong radar stealth performance to reduce the possibility of being detected. As a critical value of evaluating scattering efficiency, the radar cross section (RCS) reduction plays a pivotal role in electromagnetic stealth performance [1]. Traditional stealth methods such as surface shaping techniques [2] and radar absorbing material coatings [3] often lead to significant aerodynamic performance degradation and high energy loss for inside and outside communication. Metasurfaces, as a novel kind of two-dimensional artificial composite surfaces with specific electromagnetic responses, have garnered significant research interest in radar stealth area. These subwavelength structures allow customized beam design by manipulating the amplitude, phase and polarization of electromagnetic waves. Available applications of metasurfaces include scattering controlling [4], beam focusing [5, 6], holographic imaging [7], and orbital angular momentum (OAM) generation [8, 9]. The employment of metasurfaces offers advantages in radiation and scattering controlling with low cost, fabrication simplicity and multifunctional integration.

Vortex waves carrying orbital angular momentum have attracted significant attention in wireless communication due to their inherent modal orthogonality and unique spiral phase wavefronts. The eigenmodes of vortex waves exhibit infinite-dimensional orthogonality, and OAM-based multiplexing technology offers a novel dimension for breaking through the limits of traditional channel capacity [10]. Traditional vortex-wave generation techniques, including spiral phase plates [11,12], antenna arrays [13,14], and traveling-wave OAM antennas [15,16], are typically limited by narrow operational bandwidths, excessive losses, or restricted functionality. Metasurfaces overcome the physical limitations of these traditional approaches through sub-wavelength structure design and intelligent phase manipulation. Recent studies have

This article has been accepted for publication in IEEE Open Journal of Antennas and Propagation. This is the author's version which has not been fully edited and content may change prior to final publication. Citation information: DOI 10.1109/OJAP.2026.3729779

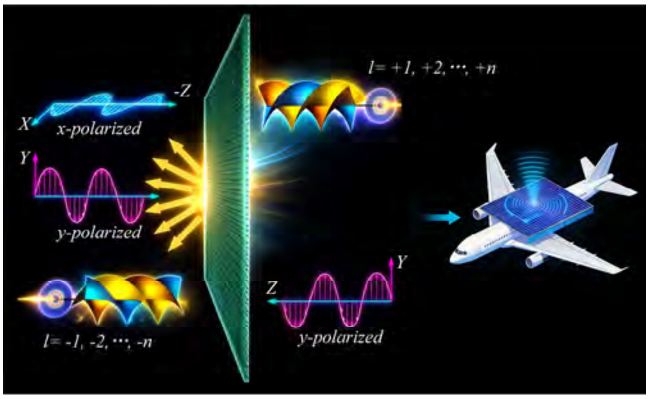

FIGURE 1. Global coordinate system and polarization- and direction-dependent operating states of the proposed metasurface.

shown that metasurface-based vortex beam generation can achieve improved bandwidth performance, higher mode purity, reduced profile thickness, and enhanced design flexibility compared with conventional approaches [17,18].

Traditional radar absorbing coatings can reduce the RCS of a platform but may also attenuate electromagnetic transmission through the platform skin. Conversely, externally mounted communication antennas introduce additional scattering and may compromise the low-observable characteristics of the platform. Existing metasurface approaches have largely addressed these two requirements independently. Polarization-conversion and phase-coding metasurfaces have been developed for scattering suppression and RCS reduction [19-22], whereas geometric-phase and frequency-selective metasurfaces have been employed to generate OAM beams with tailored polarization or frequency responses [23]. However, integrating transmissive OAM-beam generation and reflective monostatic RCS reduction within the same physical aperture remains challenging because the two functions rely on distinct polarization-dependent phase responses in the transmission and reflection channels. Moreover, the simultaneous control of the OAM order, beam propagation direction, and backward scattering distribution within a single passive aperture has not been sufficiently explored.

To address these challenges, this paper proposes a polarization-multiplexed metasurface that integrates transmissive OAM-beam generation and reflective monostatic RCS reduction within a single aperture. A global Cartesian coordinate system is adopted throughout this paper, with the metasurface located in the *xy* plane and the +*z* direction defined as shown in Fig. 1. An *x*-polarized wave incident from the +*z* side and propagating along the −*z* direction generates a transmissive OAM beam with l=+3. A *y*-polarized wave incident from the −*z* side and propagating along the +*z* direction generates a transmissive OAM beam with l=−3. For a *y*-polarized wave incident from the +*z* side and propagating along the −*z* direction, the reflected energy is redistributed to suppress the monostatic backscattering. The proposed integration is enabled by a multilayer anisotropic unit cell that provides distinct polarization-dependent transmission and

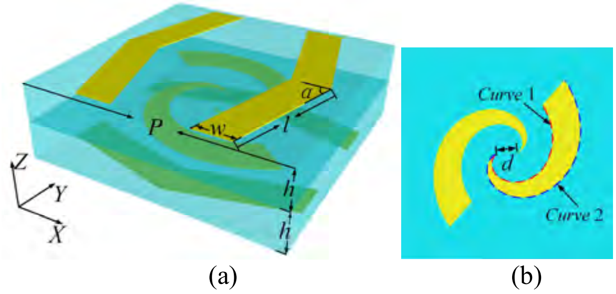

FIGURE 2. Diagram of the metasurface MS1, (a) structure of unit cell, and (b) front view of the double-spiral patch layer.

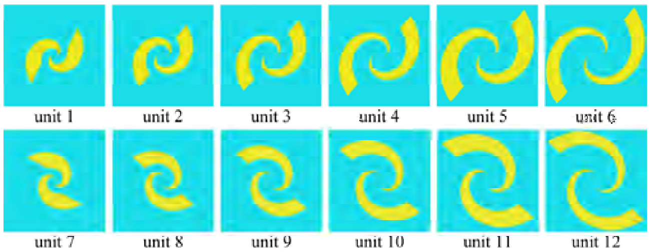

FIGURE 3. Detailed geometric shapes of 12 double equilateral helical patches.

reflection responses within the same aperture, together with a unified phase-superposition strategy in which the vortex phase is combined with a beam-deflection phase for transmissive OAM-beam generation, while the diffusion phase is superimposed with the vortex phase for monostatic RCS reduction. The resulting multifunctional behavior is investigated through full-wave simulations and measurements, including OAM-beam generation under different propagation conditions and RCS-reduction performance under both *x*- and *y*-polarized incidence.

II. COMPOSITE PHASE PRINCIPLE AND METASURFACE SIMULATION ANALYSIS

A. DESIGN OF UNIT STRUCTURE OF TRANSMISSIVE METASURFACE

A multilayer composite metasurface structure is proposed in this paper, which is designated as MS1, and the unit cell configuration is shown in Fig. 2(a). The unit cell is composed of three layers. The top layer consists of a pair of double V-shaped metallic patches which are symmetric about the *yz*-plane, serving as a polarization selector for incident waves. The middle layer contains two double spiral metallic patches, while the double V-shaped metal patches in bottom-layer are mutually perpendicular to those of the top layer. These three metallic layers are separated by two F4B dielectric substrates with a relative permittivity of 2.65 and a loss tangent of 0.002. All metallic patches are made of copper with a thickness of 0.018 mm and an electrical conductivity of σ=5.96×10^7 S/m. The optimized unit cell structure parameters are p=10 mm, h=1.5 mm, g= 0.5 mm, w=1 mm, l=3.9 mm, α=75°.

Fig. 2(b) shows the front view of the double-spiral patch layer. A single spiral patch is composed of two Archimedean spirals and a straight line connects their terminals. The two spiral patches are rotationally symmetric about the center of

This article has been accepted for publication in IEEE Open Journal of Antennas and Propagation. This is the author's version which has not been fully edited and content may change prior to final publication. Citation information: DOI 10.1109/OJAP.2026.3729779

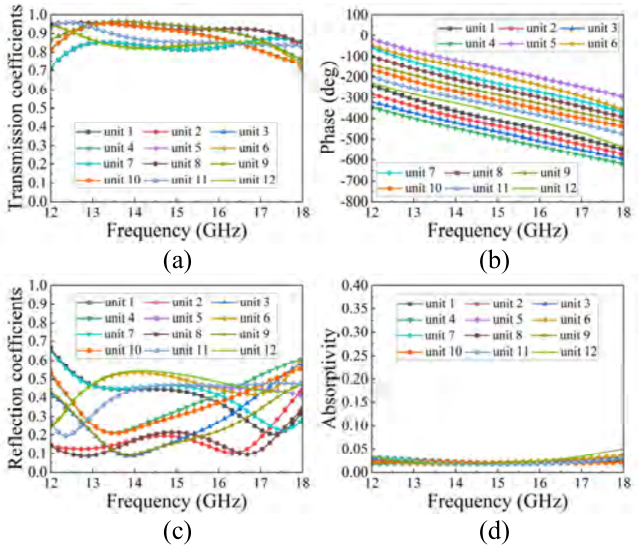

FIGURE 4. **Simulated transmission, reflection, and absorption characteristics of the 12 MS1 unit cells under normally incident *x*-polarized waves: (a) normalized magnitude of the cross-polarized transmission coefficient $|t_{yx}|$, (b) phase of t_{yx}, (c) normalized magnitude of the co-polarized reflection coefficient $|r_{xx}|$, and (d) absorptivity.**

TABLE 1. **Geometric Parameters of Double Spiral Patch (Unit: mm)**

Parameters	unit 1	unit 2	unit 3	unit 4	unit 5	unit 6
A_1	0.8	1.2	2.5	1.8	2	2.35
B_1	1.9	2	2	2	2	2
A_2	1.8	2	2.3	2.6	3	3.15
B_2	2	2	2	2	2	2

the metasurface, with the vertex spacing set as d. The polar coordinate formula for the Archimedean spiral is expressed as:

$$r_i(\phi) = \frac{A_i}{B_i}\phi, \quad \left(\phi \in [0, B_i]\right) \tag{1}$$

where A_i is the starting polar radius length of the spiral, B_i represents the total rotation radian of the spiral, and ϕ is the rotation angle in radians of a point on the spiral. The subscripts (i = 1, 2) are used to distinguish the inner and outer edges of the spiral patch.

The detailed geometric parameters of the double-spiral patches are optimized, as illustrated in Fig. 3. By adjusting the Archimedean spiral parameters, six distinct pairs of double-spiral patches with varying sizes are obtained, numbered from units 1-6, while units 7-12 are subsequently generated by rotating unit 1 to unit 6 counterclockwise by 90°. The specific geometric parameters of 12 types of double-spiral patches are shown in Table 1. Fig. 4 presents the normalized cross-polarized transmission coefficients for the 12 units of MS1 under a normally incident x-polarized wave propagating along the $-z$ direction. As shown in Fig. 4(a), the normalized magnitude of the cross-polarized transmission coefficient t_{yx} exceeds 0.8 in the range from 12.3 GHz to 17.2 GHz. This indicates that MS1 efficiently converts the incident x-polarized wave into a transmitted y-polarized wave. Similarly, MS1 can also efficiently convert a y-polarized wave propagating along the +z direction into a transmitted x-polarized wave. Fig. 4(b) shows the phase of t_{yx}, where the

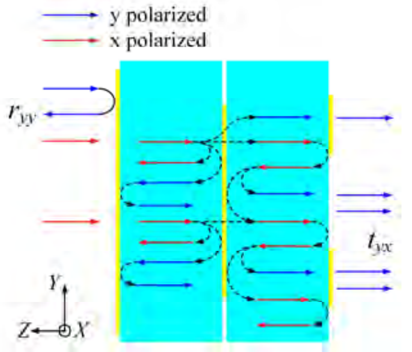

FIGURE 5. **Schematic diagram of the Fabry-Perot resonance in MS1.**

cross-polarized transmitted waves generated by MS1 with 12 units exhibit a phase gradient of approximately 30°. The successful design of 12 units of MS1 with efficient cross-polarized conversion and a gradient phase distribution covering 2π facilitates further metasurface design. To further characterize the reflection behavior and energy distribution of MS1, the co-polarized reflection coefficient and absorptivity are also evaluated, as shown in Figs. 4(c) and 4(d), respectively. For an x-polarized incident wave, the total transmittance and reflectance are calculated as $T=|t_{yx}|^2+|t_{xx}|^2$ and $R=|r_{yx}|^2+|r_{xx}|^2$, respectively, and the absorptivity is obtained from $A=1-T-R$. The calculated absorptivity remains below approximately 5% from 12 to 18 GHz and is only a few percent over most of the operating band. This indicates that the dielectric and conductor losses account for only a small fraction of the incident power. Most of the incident energy is transmitted through the cross-polarized transmission channel, while the remaining non-transmitted power is mainly reflected.

The broadband transmissive polarization conversion characteristics of MS1 are achieved using two Fabry-Perot (FP) cavities composed of three metallic layers. To explain the physical mechanism of cross-polarized transmission, Fig. 5 illustrates the quasi-Fabry-Perot resonance in MS1. The double-V wires realize polarization-selective transmission of linearly polarized waves. When a linearly polarized wave is incident on the multilayered structure, y-polarized waves are blocked and entirely reflected by the first double-V patch layer, while x-polarized waves enter the first FP resonant cavity, generating reflected co-polarized and cross-polarized waves as well as transmitted co-polarized and cross-polarized waves. The reflected waves undergo multiple reflections and interference between two metallic layers to form FP resonance. The double-V wire layer reflects generated y-polarized components back into the cavity for further interaction. The transmitted waves propagate through the double-spiral patch layer into the second FP cavity, where the y-polarized components transmit through the third double-V wire layer to complete polarization conversion. Simultaneously, the x-polarized components are reflected by the third metallic layer back into the second cavity for additional multi-reflection interference. This cascaded process ultimately converts most incident x-polarized waves into transmitted y-polarized waves. The reciprocating propagation of electromagnetic waves

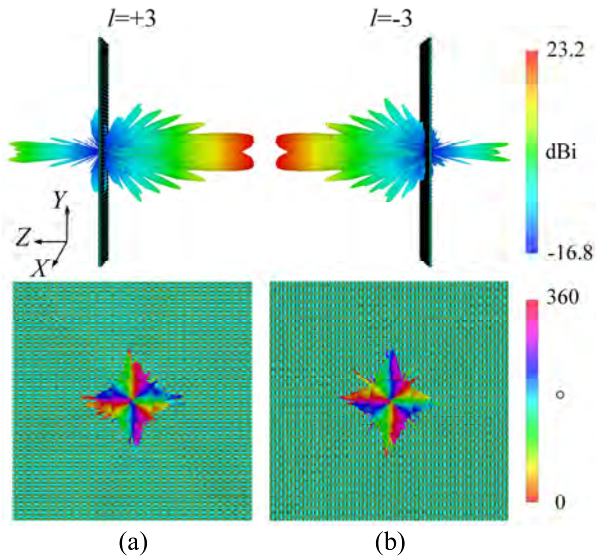

FIGURE 6. Schematic diagrams of the transmissive vortex beam generation: (a) an *l*=+3 vortex beam generated by an *x*-polarized wave propagating along the −*z* direction and (b) an *l*=−3 vortex beam generated by a *y*-polarized wave propagating along the +*z* direction.

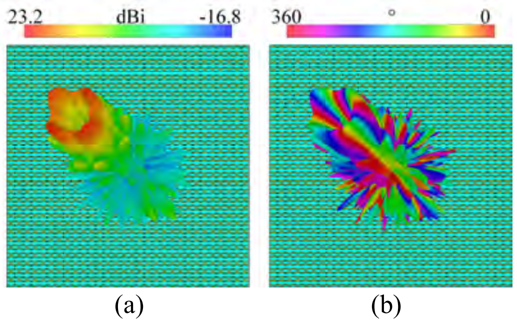

FIGURE 7. Vortex wave generated in the prescribed direction (45°, 45°) at 13.3 GHz under an *x*-polarized wave propagating along the −z direction: (a) amplitude and (b) phase distributions.

between the three metallic layers creates quasi-Fabry-Perot resonators, resulting in highly efficient transmissive polarization conversion [24, 25].

The vortex phase distribution of vortex beams generated by metasurfaces can be expressed as [26]:

$$\varphi_{\text{vortex}} = l \arctan\left(\frac{y}{x}\right) \tag{2}$$

where l is the vortex order of the generated vortex beam, and (x, y) is the position coordinates of the metasurface unit cells in the *xy*-plane, respectively. The 12 types of metasurface unit cells are arranged according to the vortex phase distribution φ_{vortex} to construct a 30×30 metasurface array. As representative examples, when an *x*-polarized wave propagates along the −*z* direction, the metasurface generates a forward-propagating vortex beam with a topological charge of l=+3 at 15 GHz, as shown in Fig. 6(a). Conversely, Fig. 6(b) shows that when a *y*-polarized wave propagates along the +*z* direction, MS1 generates an l=−3 vortex beam in the +*z* half-space. The beam phase patterns clearly demonstrate opposite phase helicity for the l = +3 and l = -3 vortex beams generated by the metasurface.

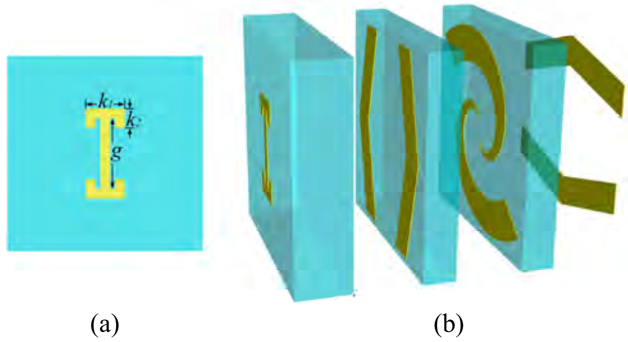

FIGURE 8. Structural diagrams of MS2 unit, (a) top view of the I-shaped patch on top layer, and (b) layered schematic diagram of the unit structure.

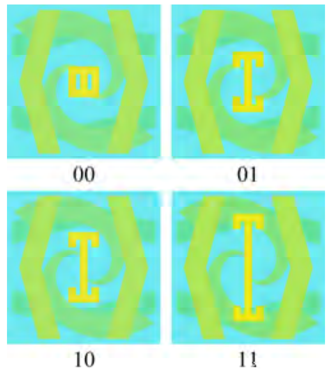

FIGURE 9. Structural perspective view of the 2-bit I-shaped coding units.

For the incident plane wave, the phase distribution of metasurface for deflecting the beam to a specified direction can be calculated by the following formula [27]:

$$\varphi_{\text{deflect}} = -\frac{2\pi}{\lambda}\sin\theta\left(x\cos\phi + y\sin\phi\right) \tag{3}$$

where λ is the wavelength, θ and ϕ are the elevation and azimuth angles of the beam emission, respectively. The linear phase-gradient term in Eq. (3) can be used not only to steer the transmitted beam toward a prescribed direction but also to compensate for the tangential phase variation introduced by a prescribed obliquely incident plane wave. The two operations share the same mathematical form, while the required gradient direction and magnitude are determined by the corresponding incidence and transmission conditions. According to the principle of phase superposition, the transmissive phase distribution of the metasurface can be obtained by superimposing the vortex phase and the beam deflection phase, which is expressed as:

$$\varphi_{\text{t}} = \varphi_{\text{vortex}} + \varphi_{\text{deflect}} \tag{4}$$

The 12 unit types are used to construct a 30×30 MS1 based on the total transmissive phase distribution φ_t with l=3 and (θ, φ) = (45°, 45°). Fig. 7 presents the simulated amplitude and phase distributions of the transmitted field under x-polarized incidence. It is demonstrated that the metasurface constructed by φ_t generates a conical vortex beam directed at (45°, 45°) at 13.3 GHz. Therefore, the designed MS1 can generate vortex beams propagating along specified directions.

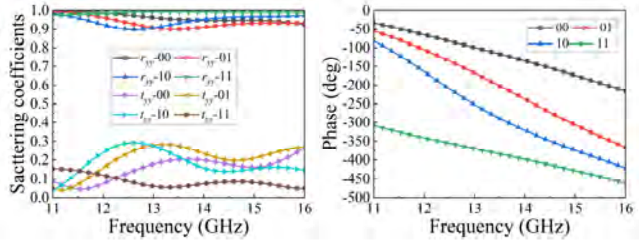

(a) (b)

FIGURE 10. Scattering characteristics of the MS2 unit under *y*-polarized wave incidence, (a) Normalized amplitudes of co-polarized reflection coefficients and transmission coefficients, and (b) Phases of co-polarized reflection coefficients.

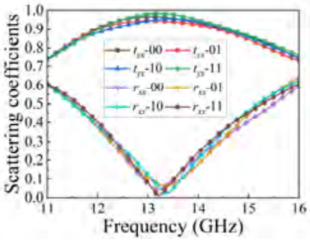

FIGURE 11. Normalized cross-polarized transmission coefficients and co-polarized reflection coefficients of the MS2 unit under *x*-polarized wave incidence.

B. DESIGN AND ANALYSIS OF MULTIFUNCTION METASURFACE

Owing to the anisotropic geometry of the V-shaped patch, MS1 completely reflects the *y*-polarized incident waves while enabling controllable transmission for the *x*-polarized waves, thereby supporting polarization-dependent vortex wave generation. To address this limitation and incorporate a scattering-suppression function, an I-shaped metallic patch is added above the top layer of the MS1 unit and separated from the double-V-shaped patch by a 2.5 mm thick F4B dielectric substrate. The resulting structure is denoted as MS2. The hierarchical schematic of the MS2 unit is shown in Fig. 8. By adjusting the long arm parameter *g* of the I-shaped patch, a set of 2-bit I-shaped coded reflective elements are obtained: 00(*g*=1 mm), 01(*g*=2.9 mm), 10(*g*=3.6 mm) and 11(*g*=6 mm), as illustrated in Fig. 9. The optimized I-shaped patch features a strip width of 0.5 mm, with k_1=2 mm and k_2=1 mm.

Fig. 10(a) shows the magnitude of the normalized co-polarized scattering coefficient for the MS2 unit under *y*-polarized wave incidence. It is evident that MS2 units can reflect most incident *y*-polarized energy. Fig. 10(b) presents the corresponding phase of the co-polarized reflection coefficient for the 2-bit I-shaped patch unit cells of MS2, which shows an approximately 90° phase gradient occurring around 13.3 GHz. The MS2 unit is derived from the MS1 configuration through the introduction of additional I-shaped metallic patches. This structural modification is intended to retain the transmissive vortex beam generation capability of MS1 while enabling enhanced manipulation of reflected waves for RCS reduction. Fig. 11 shows the normalized magnitudes of the scattering coefficients of the MS2 unit under x-polarized incidence. The results demonstrate that MS2 efficiently converts the incident *x*-polarized wave into a

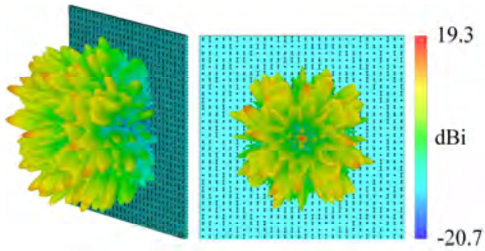

FIGURE 12. Far-field scattering pattern of MS2 under normal incidence of a *y*-polarized wave at 13.3 GHz.

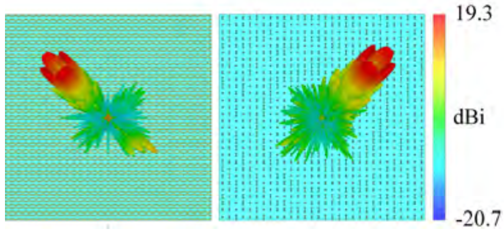

(a) (b)

FIGURE 13. Far-field patterns of vortex waves generated by MS2, (a) *x*-polarized wave propagating along the −*z* direction, and (b) *y*-polarized wave propagating along the +*z* direction.

transmitted y-polarized wave while maintaining a low co-polarized reflection level. Consequently, MS2 retains the polarization-conversion functionality of MS1 with comparable efficiency.

To design a multifunctional metasurface that integrates transmissive vortex beam generation and reflective RCS reduction, twelve double-spiral patches are arranged according to the transmissive phase matrix φ_t for generating a transmissive vortex wave, and the phase distribution of 2-bit I-shaped patches for suppressing reflection is designed. For reflective RCS reduction, a phase profile analogous to that of a parabolic lens is employed. A diffusion coefficient γ is selected for the metasurface to generate a wavefront phase of reflection approximating that of a parabolic surface. The designed diffusion phase distribution is:

$$\varphi_{\text{diffuse}} = \frac{k_0\left(x^2+y^2\right)}{\gamma} \tag{5}$$

where k_0 is the wave number. The diffusion phase uniformly diffuses the beam reflected by the metasurface into the backward space. To further enhance the monostatic RCS reduction performance, the phase superposition principle is applied to superimpose the diffusion phase with vortex phase, and the total reflection phase distribution:

$$\varphi_{\text{r}} = \varphi_{\text{diffuse}} + \varphi_{\text{vortex}} \tag{6}$$

The MS2 is constructed by arranging the double-spiral patches according to φ_t and distributing the 2-bit I-shaped patches according to φ_r (γ = 5). Fig. 12 presents the far-field scattering pattern obtained under normal incidence of a *y*-polarized wave. The results demonstrate that the MS2 redistributes the incident *y*-polarized energy into uniformly diffused scattering in the backward half-space and exhibits a distinct scattering minimum in the normal direction, thereby effectively suppressing the backscattered energy in the broadside direction. Fig. 13(a) and 13(b) display the far-field

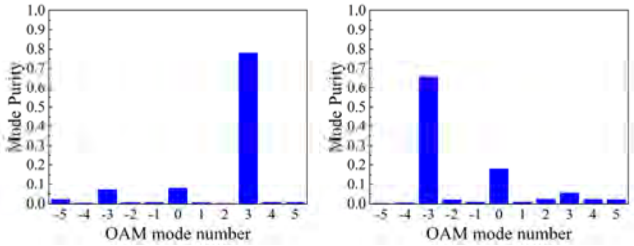

(a) (b)

FIGURE 14. Simulated OAM mode spectra of the transmissive vortex beams generated by MS2: (a) an *x*-polarized wave propagating along the −*z* direction, generating the +3-order OAM beam; and (b) a *y*-polarized wave propagating along the +*z* direction, generating the *l*=−3 OAM beam.

scattering patterns for an *x*-polarized wave propagating along the −*z* direction and a y-polarized wave propagating along the +*z* direction, respectively, from which it is seen that conical vortex beams appear on both sides of the metasurface, each featuring a central electric field null characteristic of vortex wavefronts. These results demonstrate that the metasurface can generate direction-customized transmissive vortex beams when excited by specific polarization waves, while achieving beam diffusion and monostatic RCS reduction for *y*-polarized waves propagating along the −*z* direction.

To quantitatively evaluate the OAM mode purity, the relevant cross-polarized transmitted electric field is sampled at *N* equally spaced azimuthal positions on an observation plane located 5λ from the MS2 surface. The continuous OAM modal expansion can be expressed as [28]:

$$\psi(\varphi)=\sum_{l=-\infty}^{+\infty} A_l e^{jl\varphi} \tag{7}$$

where $\psi(\varphi)$ denotes the sampled complex electric field, A_l is the complex coefficient of the *l*-th OAM mode, and $e^{jl\varphi}$ represents the helical phase of harmonic component. Because the simulated field is sampled discretely, A_l is calculated using an *N*-point discrete Fourier transform [29, 30]:

$$A_l=\frac{1}{N}\sum_{n=0}^{N-1}\psi(\varphi_n)e^{-jl\varphi_n} \tag{8}$$

where *N* is the number of azimuthal sampling points, φ_n is the angular position of the *n*-th sample, and $\psi(\varphi_n)$ is the corresponding sampled complex electric field. The normalized OAM mode purity is defined as:

$$P_l=\frac{|A_l|^2}{\sum_{k=-5}^{5}|A_k|^2} \tag{9}$$

where P_l denotes the normalized purity of the *l*-th OAM mode, and the denominator represents the total modal power over the considered OAM orders from *k*=−5 to *k*=+5. The mode purities of the vortex beams generated by an *x*-polarized wave propagating along the −*z* direction and a *y*-polarized wave propagating along the +*z* direction are calculated using Eq. (9), as shown in Fig. 14. The results show that the designed *l*=+3 and *l*=−3 components are the dominant modes in the corresponding transmission channels, with simulated mode purities of 0.78 and 0.66, respectively.

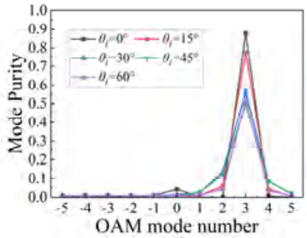

FIGURE 15. Simulated normalized OAM modal spectra of a normally transmitted *l*=+3 vortex beam under prescribed incidence angles of θ_i=0°, 15°, 30°, 45° and 60°.

Figs. 13 and 14 consider OAM beams transmitted toward the prescribed direction of θ_t=45°, for which the aperture phase includes both the vortex phase and the beam-steering phase. To evaluate oblique incidence, the incident plane wave is assumed to arrive at an angle θ_i, while the transmitted *l*=+3 OAM beam propagates along the surface-normal direction. The tangential phase variation introduced by oblique incidence is compensated using the linear phase-gradient term in Eq. (3). A separate phase distribution is synthesized for each prescribed incidence angle.

Fig. 15 shows the simulated normalized OAM spectra for θ_i =0°, 15°, 30°, 45° and 60°. The *l*=+3 component remains dominant, with mode purities of 0.878, 0.774, 0.561, 0.496 and 0.519, respectively. The mode purity exhibits an overall decreasing tendency with increasing incidence angle, although a slight recovery is observed at 60°. Because the reported mode purity is a normalized modal-power fraction, it is determined by the relative power distribution among the considered OAM modes and therefore does not necessarily vary monotonically with the incidence angle. As shown in Fig. 15, the combined power leakage into the adjacent *l*=+2 and *l*=+4 modes is lower at 60° than at 45°, which is consistent with the slight increase in the normalized *l*=+3 mode purity from 0.496 to 0.519. This nonmonotonic variation can be attributed to the combined effects of the angle-dependent unit-cell response, phase discretization, and finite-aperture effects, which redistribute power among the target and neighboring OAM modes. The higher mode purity under normal incidence compared with that in Fig. 14 is partly due to the absence of the additional phase gradient required for output-beam steering. These results demonstrate that the proposed phase-synthesis method can be adapted to a prescribed oblique incidence angle, although the overall modal performance degrades at large incidence angles.

To evaluate the angular dependence of the RCS-reduction performance, the fixed MS2 layout was analyzed at θ_i =0°, 15°, 30°, 45° and 60° without angle-dependent phase compensation, using a same-sized PEC plate under identical conditions as the reference. Unlike the angle-compensated OAM synthesis in Fig. 15, the same fixed MS2 layout is used for all incidence angles in the following RCS analysis. For each incidence angle, the monostatic RCS is evaluated in the source-return direction, whereas the specular RCS is evaluated in the corresponding mirror-reflection direction. The corresponding monostatic and specular-direction RCS-

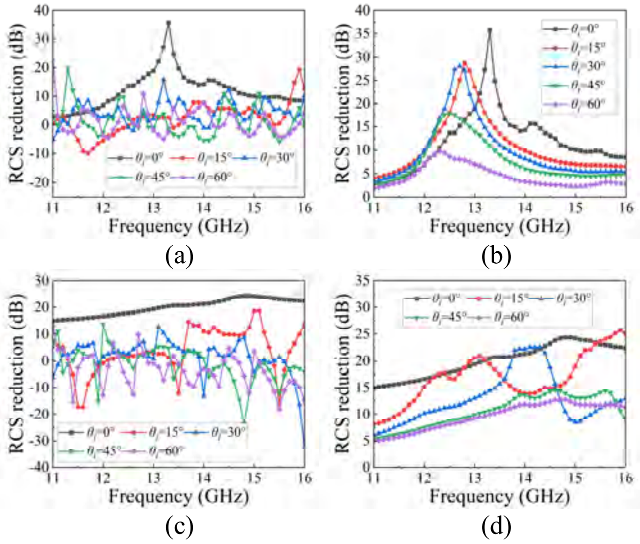

FIGURE 16. Simulated RCS reduction of the fixed MS2 metasurface under different incidence angles without angle-dependent phase compensation: (a) monostatic RCS reduction under *y*-polarized incidence; (b) specular-direction RCS reduction under *y*-polarized incidence; (c) monostatic RCS reduction under *x*-polarized incidence; and (d) specular-direction RCS reduction under *x*-polarized incidence.

reduction results for *y*- and *x*-polarized incidence are shown in Fig. 16. Under oblique incidence, the dominant reflection of the PEC reference shifts toward the specular direction, substantially reducing its monostatic backscattering; consequently, the PEC-referenced monostatic RCS reductions for both polarizations fluctuate around 0 dB at large incidence angles. In the specular direction, the *y*-polarized RCS reduction generally decreases with increasing angle and is mostly below 10 dB at 60°, because the additional tangential incident phase and angle-dependent unit-cell response perturb the designed diffusion-vortex reflection phase. For *x*-polarized incidence, appreciable specular-reflection suppression is retained, but the reduction also generally decreases at large angles as the uncompensated incident phase and angular response increasingly perturb the designed polarization-conversion transmission and OAM wavefront. These results indicate that the fixed passive layout is primarily optimized for normal and near-normal incidence.

III. FABRICATION AND EXPERIMENTAL VALIDATION

To experimentally validate the transmissive vortex beam generation and RCS reduction performance of the proposed diffusion-vortex composite phase metasurface, a 300 mm × 300 mm MS2 sample is fabricated and tested in an anechoic chamber. For the RCS reduction evaluation, a 300 mm × 300 mm PEC plate, having the same aperture dimensions as MS2, is used as the reference target. The PEC plate and MS2 are simulated and measured under identical polarization, distance, and angular conditions. Because the finite size of the chamber does not satisfy the far-field condition for plane-wave illumination, a horn antenna is used as the feeding source. A compensation phase is therefore superimposed on the metasurface phase distribution to convert the quasi-spherical

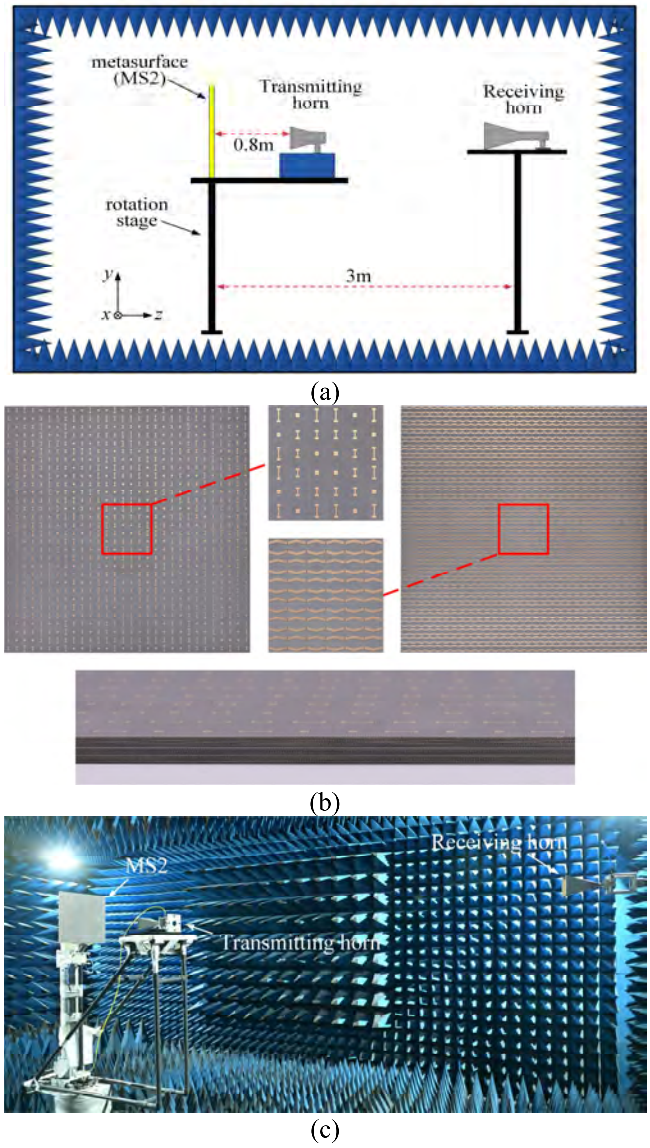

FIGURE 17. Fabrication and RCS measurement of MS2: (a) schematic illustration of the measurement geometry and coordinate system; (b) front and back views of the fabricated metasurface with enlarged unit-cell details; and (c) anechoic chamber measurement setup.

wavefront emitted by the horn into an equivalent planar wavefront. The required phase delay for compensating the path-length difference between the horn aperture and each metasurface unit cell is given by:

$$\varphi_{comp} = k_0\left(\sqrt{x^2 + y^2 + z_0^{\ 2}} - z_0\right) \tag{10}$$

where z_0=0.8 m is the normal distance from the aperture of the transmitting horn antenna to the metasurface. The phase distributions of double-spiral patches and 2-bit I-shaped patches in the finally fabricated MS2 metasurface array are φ_t+φ_{comp} and φ_r+φ_{comp}, respectively.

As shown in Fig. 17(a), the MS2 sample and the transmitting horn were mounted on the same rotating stage, while the receiving horn was fixed on a separate frame. Therefore, the incident wave always illuminated the sample at normal incidence during the angular scan. In the sample

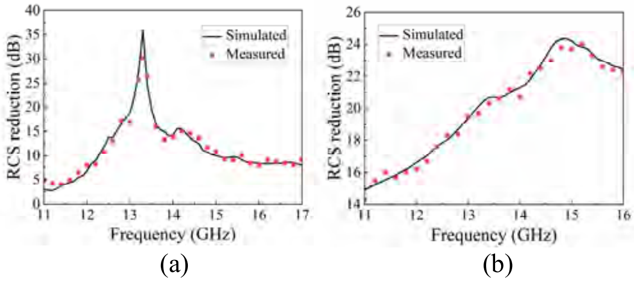

FIGURE 18. Simulated and measured monostatic RCS reductions of MS2 with respect to a same-sized PEC plate under normally incident waves propagating along the −*z* direction: (a) *y*-polarized incidence; (b) *x*-polarized incidence.

coordinate system, the metasurface was placed in the *xy* plane, and the incident wave propagated along the −*z* direction,corresponding to θ_i=0°. The receiving angle θ_r was defined with respect to the +*z* broadside direction. Fig. 17(b) shows the front and back views of the fabricated metasurface, while Fig. 17(c) illustrates the anechoic chamber testing environment. An Agilent Technologies E8363C PNA network analyzer is connected to a Ceyear 80243 microwave power amplifier to increase the transmitted power and improve the signal-to-noise ratio. Two horn antennas are used as the transmitting and receiving antennas.

Fig. 18(a) presents the simulated and measured monostatic RCS reductions under normally incident y-polarized waves. The measured RCS reduction exceeds 10 dB from 12.4 GHz to 15.6 GHz and reaches a maximum of 30.15 dB at 13.3 GHz. The measured and simulated results exhibit consistent frequency-dependent trends. Fig. 18(b) presents the simulated and measured RCS-reduction results under normally incident *x*-polarized waves. MS2 also exhibits significant monostatic RCS reduction for *x*-polarized incidence. The measured RCS reduction is approximately 15–24 dB over the measured frequency from 11 GHz to 16 GHz, with a peak value of approximately 24 dB near 15 GHz. The simulated and measured results show good agreement. The RCS-reduction mechanism under *x*-polarized incidence is different from that under *y*-polarized incidence. For *x*-polarized incidence, the incident energy is mainly coupled into the transmissive polarization conversion channel. Therefore, the co-polarized reflected field is suppressed, and a considerable portion of the incident energy is transmitted as a cross-polarized vortex beam.

For the bistatic measurement, the RCS was calibrated by the substitution method using a same-sized PEC plate as the reference target. Fig. 19 presents the simulated and measured bistatic RCS patterns of MS2 under three polarization and propagation conditions. As shown in Fig. 19(a), for an *x*-polarized wave propagating along the −*z* direction, both the simulated and measured patterns exhibit a pronounced broadside null and off-axis maxima, which are consistent with the angular characteristics of the designed transmissive l=+3 OAM beam. For the *y*-polarized wave propagating along the −*z* direction, Fig. 19(b) shows that the broadside backscattering is effectively suppressed, while the reflected energy is redistributed toward off-normal directions,

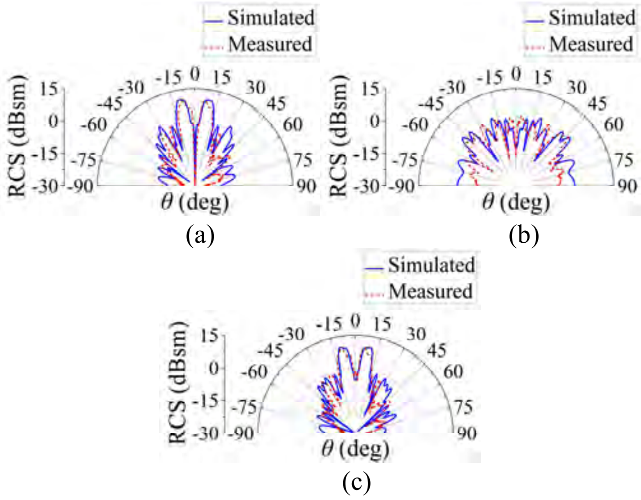

FIGURE 19. Simulated and measured bistatic RCS patterns of MS2 under different incidence conditions: (a) an *x*-polarized wave propagating along the −*z* direction, (b) a *y*-polarized wave propagating along the −*z* direction, and (c) a *y*-polarized wave propagating along the +*z* direction.

confirming the designed monostatic RCS-reduction response. When the *y*-polarized wave propagates along the +*z* direction,the patterns in Fig. 19(c) again exhibit a broadside null and off-axis maxima, in agreement with the simulated response of the designed transmissive l=−3 OAM beam. Overall, the measured results agree well with the simulations and verify the polarization- and direction-dependent transmission and scattering characteristics of the proposed metasurface.

IV. CONCLUSIONS

This paper presents a polarization-multiplexed metasurface that integrates transmissive OAM-beam generation and reflective monostatic RCS reduction within a single aperture. The integrated functionality is realized using a multilayer anisotropic unit cell that provides polarization-dependent transmission and reflection responses, together with a unified phase-superposition strategy for the two channels. Depending on the polarization and propagation direction of the incident wave, the metasurface generates +3- and −3-order transmissive OAM beams or suppresses the monostatic backscattering. Simulated modal analyses confirm the intended OAM states under normal and prescribed deflected propagation conditions, while the measurements verify the corresponding beam and scattering characteristics. Under normally incident y-polarized waves, the measured RCS reduction exceeds 10 dB from 12.4 GHz to 15.6 GHz and reaches a maximum of 30.15 dB at 13.3 GHz. Under normally incident *x*-polarized waves, the measured RCS reduction is approximately 15–24 dB from 11 GHz to 16 GHz. These results demonstrate that polarization-dependent transmission and reflection functions can be integrated within the same metasurface aperture, providing a potential approach for combined electromagnetic scattering control and direction-dependent OAM communication.

REFERENCES

[1] G. Y. Deng, Y. H. Zhang, H. T. Gao, Y. L. Shu, S. Y. He and G. Q. Zhu, "A super diffuse broadband RCS reduction surface design based on rotated phase coding polarization conversion metasurfaces," IEEE Trans. Antennas Propag., vol. 71, no. 9, pp. 7409–7417, Sep. 2023.

[2] W. F. Bahret, "The beginnings of stealth technology," IEEE Trans. Aerosp. Electron. Syst., vol. 29, no. 4, pp. 1377-1385, Oct. 1993.

[3] A. A. Khurram, N. Ali, S. A. Rakha, P. Zhou and A. Munir, "Optimization of the carbon coating of honeycomb cores for broadband microwave absorption," IEEE Trans. Electromagn. Compat., vol. 56, no. 5, pp. 1061-1066, Oct. 2014.

[4] M. K. T. Al-Nuaimi, G. L. Huang, W. G. Whittow, D. Wang, R. S. Chen and S. W. Wong, "Coding engineered reflector for wide-band RCS reduction under wide angle of incidence," IEEE Trans. Antennas Propag., vol. 70, no. 10, pp. 9947-9952, Oct. 2022.

[5] Z. X. Zhu and X. Zhou, "Study on electromagnetic focusing with fully phase-adjustable high transmittance metasurface," Electronics, vol. 14, no. 4, p. 669, Feb. 2025.

[6] H. Xiong, J. Y. Xie, J. H. Deng, Q. Yang, M. Suo and H. Q. Zhang, "Design and implementation of a near-field focused metasurface for microwave power transmission," Results Phys., vol. 55, p. 107159, Nov. 2023.

[7] G. Y. Qu, W. H. Yang, Q. H. Song, Y. L. Liu, C. W. Qiu, J. C. Han, D. P. Tsai and S. M. Xiao, "Reprogrammable meta-hologram for optical encryption," Nature Commun., vol. 11, no. 1, p. 5484, Oct. 2020.

[8] C. Ji, J. K. Song, C. Huang, X. Y. Wu and X. G. Luo, "Dual-band vortex beam generation with different OAM modes using single-layer metasurface," Opt. Express, vol. 27, no. 1, pp. 34–44, Jan. 2019.

[9] D. Zhang, J. W. Che, C. H. He, X. Zou, Q. Chen, L. Zhang, Z. B. Zhu and F. L. Yu, "Backscattering enhancement of a chessboard metasurface based on the orbital angular momentum detection approach," Opt. Mater. Express, vol. 13, no. 7, pp. 1947–1955, Jul. 2023.

[10] R. Wang, M. Wang, Y. Zhang, D. Liao, and L. Jing, "Generation of orbital angular momentum multiplexing millimeter waves based on a circular traveling wave antenna," Opt. Express, vol. 31, no. 3, pp. 5131–5139, Jan. 2023.

[11] X. N. Hui, S. L. Zheng, Y. P. Hu, C. Xu, X. F. Jin and H. Chi, "Ultralow reflectivity spiral phase plate for generation of millimeter-wave OAM beam," IEEE Antennas Wireless Propag. Lett., vol. 14, pp. 966-969, Jan. 2015.

[12] Z. F. Zhang, S. L. Zheng, W. T. Zhang, X. F. Jin, H. Chi and X. M. Zhang, "Experimental demonstration of the capacity gain of plane spiral OAM-based MIMO system," IEEE Microwave Wireless Compon. Lett., vol. 27, no. 8, pp. 757-759, Apr. 2017.

[13] S. M. Mohammadi, L. K. S. Daldorff, J. E. S. Bergman, R. L. Karlsson, B. Thide and K. Forozesh, "Orbital angular momentum in radio—a system study," IEEE Trans. Antennas Propag., vol. 58, no. 2, pp. 565-572, Feb. 2010.

[14] B. Y. Liu, Y. H. Cui and R. L. Li, "A broadband dual-polarized dual-OAM-mode antenna array for OAM communication," IEEE Antennas Wireless Propag. Lett., vol. 16, pp. 744-747, Aug. 2017.

[15] F. Shen, J. Mu, K. Guo, S. M. Wang and Z.Y. Guo, "Generation of continuously variable-mode vortex electromagnetic waves with three-dimensional helical antenna," IEEE Antennas Wireless Propag. Lett., vol. 18, pp. 1091-1095, Mar. 2019.

[16] Z. F. Zhang, S. L. Zheng, X. F. Jin, H. Chi, X. M. Zhang, "Generation of plane spiral OAM waves using traveling-wave circular slot antenna," IEEE Antennas Wireless Propag. Lett., vol. 16, pp. 8-11, Apr. 2017.

[17] H. X. Xu, H. W. Liu, X. H. Ling, Y. M. Sun and F. Yuan, "Broadband vortex beam generation using multimode Pancharatnam–Berry metasurface," IEEE Trans. Antennas Propag., vol. 65, no. 12, pp. 7378-7382, Dec. 2017.

[18] G. W. Ding, K. Chen, X. Y. Luo, J. M. Zhao, T. Jiang and Y. J. Feng, "Dual-Helicity decoupled coding metasurface for independent spin-to-orbital angular momentum conversion," Phys. Rev. Appl., vol. 11, no. 4, pp. 044043, Apr. 2019.

[19] Z. H. Li, J. H. Wang and W. Zheng, "Deformable transparent metasurface with multipolarization absorptive characteristics for RCS reduction," IEEE Trans. Antennas Propag., vol. 73, no. 3, pp. 1768-1776, Mar. 2025.

[20] Y. T. Jia, Y. Liu, Y. J. Guo, K. Li and S. X. Gong, "Broadband polarization rotation reflective surfaces and their applications to RCS reduction," IEEE Trans. Antennas Propag., vol. 64, no. 1, pp. 179-188, Jan. 2016.

[21] Q. Liu, H. Y. Chen, Y. Y. Yan, X. Yao, D. F. Liang, J. L. Xie and L. J. Deng, "RCS reduction metasurface based on orbital angular momentum," Results Phys., vol. 53, p. 107008, Sep. 2023.

[22] L. J. Zhang, C. Gao, H. Guo, H. Y. Zhang, Z. P. Zhao and T. Liu, "Efficient polarization conversion metasurface for scattered beam control and RCS reduction," Sci. Rep., vol. 14, p. 26260, Nov. 2024.

[23] P. Xu, K. Y. Zhang, H. X. Liu, R. J. Li and L. Li, "Dual-band metasurface generating multiple OAM beams independently in full polarizations," Opt. Express, vol. 31, no. 20, pp. 32637–32651, Sep. 2023.

[24] Z. Y. Xiao, D. J. Liu, X. L. Ma and Z. H. Wang, "Multi-band transmissions of chiral metamaterials based on Fabry-Perot like resonators," Opt. Express, vol. 23, no. 6, pp. 7053-7061, Mar. 2015.

[25] K. K. Xu, Z. Y. Xiao, J. T. Tang, D. J. Liu and Z. H. Wang, "Ultra-broad band and dual-band highly efficient polarization conversion based on the three-layered chiral structure," Physica E, vol. 81, pp. 169-176, Jul. 2016.

[26] P. C. Tang, L. M. Si, Q. Q. Yuan, J. Tian, J. X. Deng, T. Y. Ma, X. Bao, C. He, and W. R. Zhu, "Dynamic generation of multiplexed vortex beams by a space-time-coding metasurface," Photon. Res., vol. 13, no. 1, pp. 225–234, Jan. 2025.

[27] S. Wu, Y. H. Zhang, X. D. Cui, J. Y. Zhang, P. Xu and X. Ji, "Generation of dual-polarization orbital angular momentum vortex beams with reflection-type metasurface," Opt. Commun., vol. 553, p. 130107, Feb. 2024.

[28] L. J. Yang, S. Sun and W. E. I. Sha, "Ultrawideband reflection-type metasurface for generating integer and fractional orbital angular momentum," IEEE Trans. Antennas Propag., vol. 68, no. 3, pp. 2166-2175, Mar. 2020.

[29] Q. Feng, J. Liang, and L. Li, "Variable scale aperture sampling reception method for multiple orbital angular momentum modes vortex wave," IEEE Access, vol. 7, pp. 158847–158857, Dec. 2019.

[30] W. Zhang, S. Zheng, Y. Chen, X. Jin, H. Chi, and X. Zhang, "Orbital angular momentum-based communications with partial arc sampling receiving," IEEE Commun. Lett., vol. 20, no. 7, pp. 1381–1384, Jul. 2016.